

## Article

# Assessment of Energy Conversion in Passive Components of Single-Phase Photovoltaic Systems Interconnected to the Grid

Heriberto Adamas-Pérez , Mario Ponce-Silva \* , Jesús Darío Mina-Antonio , Abraham Claudio-Sánchez   
and Omar Rodríguez-Benítez

Tecnológico Nacional de México-CENIDET, Cuernavaca 62490, Mexico

\* Correspondence: mario.ps@cenidet.tecnm.mx

**Abstract:** This paper presents a mathematical analysis of how energy return in grid-connected single-phase photovoltaic systems affects the sizing of passive components. Energy return affects the size of the link capacitor, making it larger than reported in the literature. One of the main points of this article is that an inverter connected to the grid using a DC–DC converter with an appropriate link capacitor is analyzed. The energy return is caused by the value (in Henry units) of the L-filter, which is also analyzed in this paper. The analysis shows that there is a link between the value of the L-filter and the voltage of the DC bus. The analysis assumes two conditions: (1) the DC bus voltage is always higher than the peak value of the grid sinusoidal voltage, and (2) there is a unity power factor at the connection point between the grid and the L-filter. To operate in an open loop, a compensation phase angle is calculated and introduced in the single-phase inverter modulation; this phase angle compensates the phase shift caused by the L-filter, avoiding the use of a phase-locked-loop (PLL) control system. The L-filter ripple current is evaluated by Fourier analysis, and the DC bus ripple voltage is evaluated by considering the energy returned to the link capacitor. The results of the analyses are compared with existing methods reported in the literature. The results also show that, to minimize the value of the L-filter, the DC voltage must be almost equal to the maximum voltage of the grid. Equations to assess the value of the DC-link capacitor and the L-filter in function of their ripples are developed. The results were verified with simulations in Simulink and experimentally.

**Keywords:** capacitors; DC–DC converters; DC–AC power converters; solar energy; passive filters; power systems



**Citation:** Adamas-Pérez, H.; Ponce-Silva, M.; Mina-Antonio, J.D.; Claudio-Sánchez, A.; Rodríguez-Benítez, O. Assessment of Energy Conversion in Passive Components of Single-Phase Photovoltaic Systems Interconnected to the Grid. *Electronics* **2023**, *12*, 3341. <https://doi.org/10.3390/electronics12153341>

Academic Editors: José Manuel Ribeiro Baptista and Tiago Pinto

Received: 19 June 2023

Revised: 30 July 2023

Accepted: 2 August 2023

Published: 4 August 2023



**Copyright:** © 2023 by the authors. Licensee MDPI, Basel, Switzerland. This article is an open access article distributed under the terms and conditions of the Creative Commons Attribution (CC BY) license (<https://creativecommons.org/licenses/by/4.0/>).

## 1. Introduction

Solar energy is considered almost infinite; however, its great disadvantage is the intermittency of its generation. In general, solar energy is converted by photovoltaic panels (PVs) into electrical energy, which is interconnected through power converters to the grid or isolated loads. This set of elements is called a photovoltaic system [1–3].

PVs have a lifetime of 20 to 30 years, while the lifetime of PV inverters is usually limited to less than 15 years [4,5]. Therefore, power converters with high reliability are needed [6]. In a single-phase photovoltaic system, the power conversion from DC to AC requires a link capacitor to compensate the power variations [7–10]. The electrolytic capacitor is known to be a limiting component in the reliability and lifetime of a photovoltaic system [11–13]. Recently, several new topologies have been proposed that do not use electrolytic capacitors [14–17]. Previous research has yielded mathematical expressions to assess the DC bus link capacitor for photovoltaic systems [18–20]. In addition, in recent years, computational intelligence, artificial intelligence, and machine learning algorithms have been used. These techniques have been widely used in the generation of energy from renewable sources [21–24].

A typical schematic of a photovoltaic system is shown in Figure 1. The conventional analysis to evaluate the DC-link capacitor assumes that energy always flows from the

DC bus to the inverter. This will be true if passive filters, such as the L-filter, are not necessary and are not placed between the grid and the inverter. However, these passive filters are necessary to block the harmonics generated by the inverter. The addition of these filters causes a phase shift between the voltage delivered by the inverter and the grid voltage. Commonly, this phase shift and other variations are compensated with a PLL. The PLL maintains a unitary power factor in the grid. Nevertheless, the phase shift causes a non-unity power factor at the connection point between the inverter and the passive filter. Therefore, there will be reactive power back to the inverter and to the DC bus. This situation could be worse if, at the point of connection to the grid, the power factor is non-unity, which would result in a higher power return to the link capacitor. The use of PLL does not avoid this return of energy to the link capacitor; the traditional solution to this problem is to choose a capacitor large enough to absorb the returned energy and to maintain the ripple of the DC-bus voltage low.

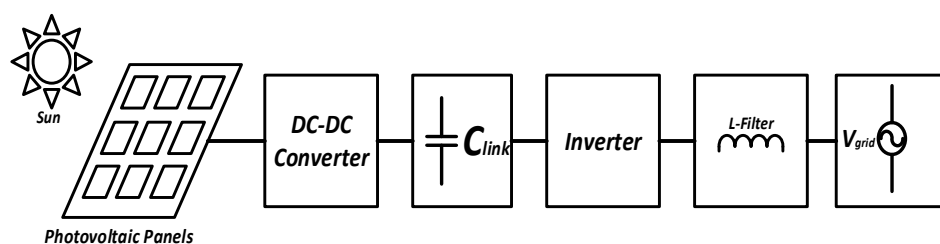


**Figure 1.** Photovoltaic system.

With respect to the passive filter added to block the harmonics of the inverter, it is usually calculated using bode diagrams, but this procedure does not consider the effect of these components on the DC-bus voltage and the link capacitor. This paper analyzes the energy flow from the link capacitor to the grid to assess the effect of the L-filter on the DC-bus voltage and the link capacitor. The analysis considers the ripple of current in the L-filter and the ripple of voltage in the link capacitor as functions of the nominal power injected into the grid, considering the following conditions:

1. The DC bus voltage is always higher than the peak value of the sinusoidal grid voltage.
2. There is a unity power factor at the connection point between the grid and the L-filter.

The first condition is to avoid the grid delivering energy to the L-filter and the inverter. These analyses have not been reported in the literature, so this is the main contribution of the paper. The analysis is carried out for specific operation points defined by the specifications, so the system is operating in an open loop without the use of a PLL. This is necessary to observe the energy flow in the system without any perturbation. This condition does not imply that one should always avoid the use of the PLL; the analysis involves first designing the open loop operation with more precision and then adding the PLL to compensate perturbations in the system. However, the operation will be optimized for the nominal operating conditions.

Theoretical calculations are validated with simulations in Simulink; the simulation is performed in an open loop by adjusting the switching angle of the MOSFETs of the inverter, thus emulating the operation of a control system for synchronization with the grid with a unity power factor. The paper is organized as follows: Section 2 presents an analysis of the effects caused by the L-filter in PV systems. Section 3 presents the assessment of the link capacitor as a function of the returning current from the inverter to the coupling capacitor. In Section 4, an isolated Cuk converter is designed and implemented as a DC–DC converter to supply the link capacitor. The simulation results are provided in Section 5, and Section 6 presents the experimental validation. Finally, Sections 7 and 8 present the discussion and conclusion of this work.

## 2. Effects of the L-Filter in Photovoltaics Systems

The blocks in Figure 1 show a commercial photovoltaic system. The DC-generated voltage of the PV is boosted with the DC–DC converter, and the capacitor  $C_{link}$  is the link between the DC–DC converter and the inverter. Moreover, the grid-connected inverters use a filter to obtain an injected current with a low THD. In this case, the analyzed system uses an L-filter, an isolated Cuk converter as a DC–DC converter, and a single-phase full-bridge as an inverter (see Figure 2).

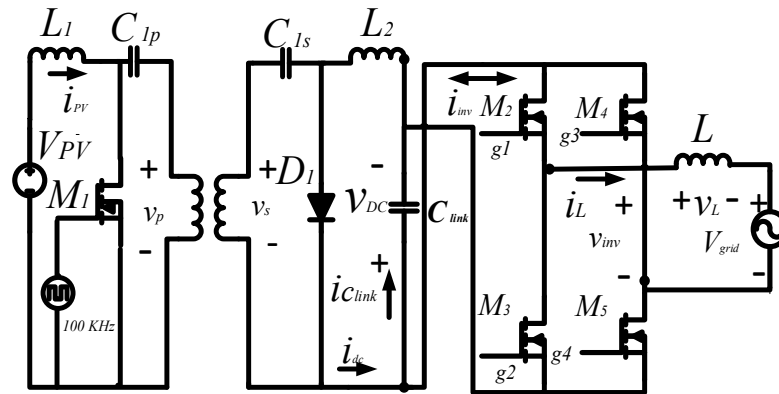


Figure 2. Isolated Cuk converter and full-bridge inverter connected to the grid with an L-filter.

Figure 3 shows the control diagram of the gates of the MOSFETs of the full-bridge inverter. It is the control that will be used in the experimental part of this article.

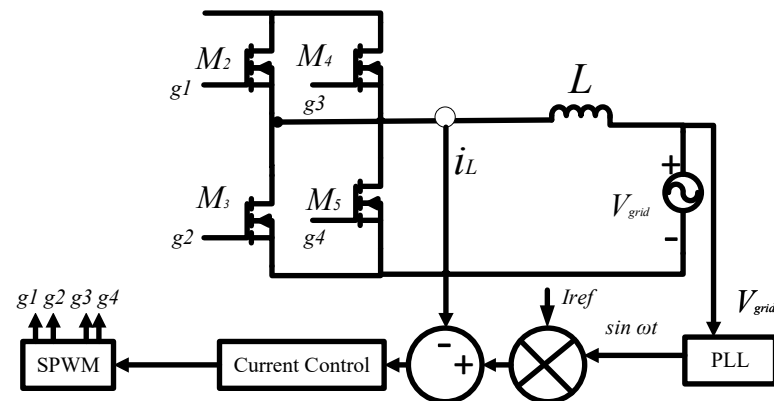
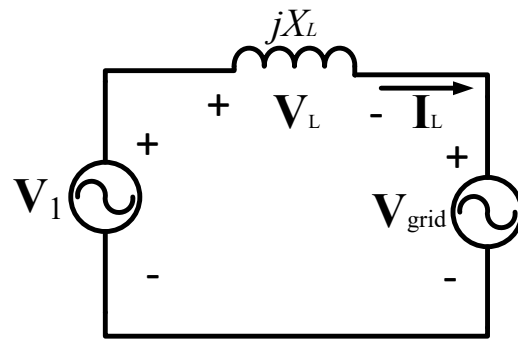


Figure 3. Block diagram of full-bridge inverter control.

In the literature, there is very little information about how to calculate the L-filter and there are no mathematical expressions for its calculation. The articles found [25–30] introduce the analysis and present the L-filter value but do not explain how they obtained it. They mention that the high value is based on a cutoff frequency that must be much larger than the grid frequency and show the Bode diagrams for a proposed value [25,28,29,31,32].

To analyze the effect of the inductor L in the assessment of the DC-level bus voltage, a simplified circuit is used (see Figure 4). For simplicity, in this circuit only the fundamental component in the inverter output voltage is considered, and a phasor analysis is applied, where  $V_1$  represents the phasor of  $v_{inv}$ ,  $v_L$  represents the inductor voltage,  $XL = \omega L$  is the reactance, and  $V_{grid}$  represents the phasor of the main grid voltage ( $v_{grid} = V_{grid} \sin(\omega t)$ ). As it was pointed out, all the analysis is carried out at the fundamental components of  $f = 60 \text{ Hz}$  or  $\omega = 2\pi f$ , and  $I_L$  is the phasor of the current injected into the grid. The reference for all the phasors is the grid voltage.



**Figure 4.** L-filter connected to the grid.

### 2.1. Output Current Due to Fundamental Components in the Inverter Output Voltage

The analysis of the circuit voltages of the series connection in Figure 3 is undertaken with the grid frequency set so that  $V_1$  is the magnitude of voltage at the fundamental frequency of the sinusoidal pulse width modulation (SPWM). The inductor voltage ( $V_L$ ) is substituted by the multiplication of the inductive reactance ( $X_L$ ) with  $I_L$  and an imaginary number ( $j$ ). The fundamental voltage  $V_1$  can be obtained from (1) by expressing it in polar form, where  $V_1$  is the magnitude of the phasor  $\mathbf{V}_1$ . This is shown in Equation (1):

$$\mathbf{V}_1 = \mathbf{V}_{grid} + (jX_L \mathbf{I}_L) = V_1 \angle \phi_{inv} \quad (1)$$

The magnitude and phase of Equation (1) are obtained, as shown in Equations (2) and (3):

$$V_1 = |\mathbf{V}_1| = \sqrt{V_{grid}^2 + (I_L X_L)^2} \quad (2)$$

$$\phi_{inv} = \tan^{-1} \left( \frac{I_L X_L}{V_{grid}} \right) \quad (3)$$

The angle  $\phi_{inv}$  is the lag phase angle that must be added to the inverter output voltage to obtain a unity power factor at the connection point with the grid. Assuming that  $I_L$  must be in phase with the grid voltage  $V_{grid}$  to obtain a unity power factor at the connection point and that  $I_L$  is a pure sinusoidal waveform, the average power  $P_{avg}$  can then be calculated using Equation (4):

$$P_{avg} = \frac{I_L}{\sqrt{2}} \frac{V_{grid}}{\sqrt{2}} \cos(0^\circ) = \frac{I_L V_{grid}}{2} \quad (4)$$

Solving  $I_L$  from Equation (4) results in Equation (5):

$$I_L = \frac{2P_{avg}}{V_{grid}} \quad (5)$$

### 2.2. Output Current Due to Harmonic Components in the Inverter Output Voltage

To determine the harmonic content of the inverter output voltage, a relationship between the frequency of the triangular carrier signal  $f_{sw}$  of the SPWM modulation and the frequency of the grid  $f_{grid}$  is defined. This relationship will be called  $\beta$ , and it is shown in Equation (6):

$$\beta = \frac{f_{sw}}{f_{grid}} \quad (6)$$

To calculate the harmonics of a unipolar SPWM signal, the Fourier series is used [33–35]. In a unipolar SPWM modulation, there are only odd harmonics, and the DC component is equal to 0. The Fourier series of a unipolar SPWM signal [35,36] is shown in Equations (7) and (8):

$$v_n = \frac{4V_{dc}}{n\pi} \sum_{k=1}^N (-1)^{k+1} \cos(na_k) \quad (7)$$

$$n = (2\beta - 1), (2\beta + 1), (4\beta - 1), (4\beta + 1), (6\beta - 1), (6\beta + 1) \dots \tag{8}$$

where  $V_{dc}$  is the average amplitude of the DC bus,  $N$  is the number of switching angles per quarter of the signal period,  $a_k$  are the switching angles for a quarter-period signal and are conditioned as shown in Equation (9), and  $k$  is the  $k$ -th switching angle.

$$a_1 < a_2 < \dots < a_N < \frac{\pi}{2} \tag{9}$$

By obtaining the switching angles and solving Equation (7) for the harmonic  $n_{sw} = 2\beta + 1$ , it is possible to obtain the maximum output voltage at the harmonic  $n_{sw}$  ( $V_{nsw}$ ) as a function of ( $V_{dc}$ ), as shown in Equation (10), where  $m_{nsw}$  is the relationship between the maximum output voltage at the harmonic  $n_{sw}$  ( $V_{nsw}$ ) and ( $V_{dc}$ ). For a modulation index, this is equal to 1.

$$m_{nsw} = \frac{V_{nsw}}{V_{dc}} = 0.176 \tag{10}$$

For this work, the unipolar SPWM modulation technique was used with a carrier switching frequency  $f_{sw} = 15$  kHz, where the harmonics after the fundamental appear at a frequency of  $2\beta + 1$ ,  $2\beta - 1$ ,  $2\beta + 2$ , and  $2\beta - 2$ , respectively. The harmonic  $2\beta + 1$  ( $n_{sw}$ ) is one of the largest harmonics and is the inverter output voltage ( $v_{inv}$ ) at the frequency of the harmonic  $n_{sw}$  ( $f_{nsw}$ ). To evaluate the magnitude of the current at harmonic  $n_{sw} = 2\beta + 1$ , a phasor analysis is again used. For this harmonic, the circuit is simplified to the circuit of Figure 5, where  $V_{nsw}$  represents the voltage phasor at the inverter output at harmonic  $n_{sw}$ ,  $V_{Lnsw}$  represents the inductor voltage at the same harmonic,  $X_{Lnsw} = \omega_{nsw}L$  is the reactance in the same harmonic  $n_{sw}$ , and  $I_{Lnsw}$  is the phasor of the current at harmonic  $n_{sw}$ . Given that  $V_{grid}$  has only the fundamental frequency (60 Hz) and does not have harmonic components, it is no longer included in the analysis of  $I_{Lnsw}$  current.

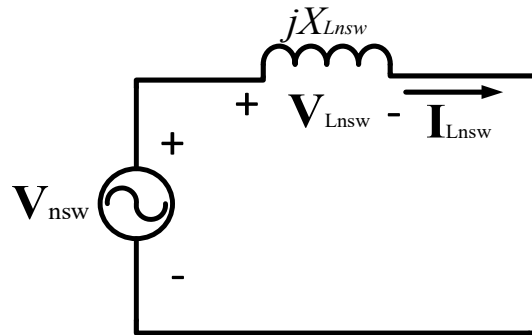


Figure 5. L-filter on harmonic  $n_{sw} = 2\beta + 1$ .

Applying the Kirchhoff voltage law to the circuit of Figure 4 and substituting the inductor voltage ( $V_{Lnsw}$ ) by the equivalent product of the inductive reactance ( $X_{Lnsw}$ ) with  $I_{Lnsw}$  gives Equation (11):

$$V_{nsw} - (jX_{Lnsw}I_{Lnsw}) = 0 \tag{11}$$

Subtracting the current phasor ( $I_{Lnsw}$ ) from Equation (11) gives Equation (12):

$$I_{Lnsw} = \frac{V_{nsw}}{jX_{Lnsw}} \tag{12}$$

The magnitude  $I_{Lnsw}$  is obtained from Equation (12). This is shown in Equation (13):

$$I_{Lnsw} = |I_{Lnsw}| = \frac{V_{nsw}}{X_{Lnsw}} \tag{13}$$

where  $X_{Lnsw}$  is the inductive reactance at harmonic  $n_{sw}$ . This can be calculated with Equation (14):

$$X_{Lnsw} = \omega_{nsw}L \tag{14}$$

### 2.3. Calculation of the L-Filter from the Ripple Current

For this analysis, the current harmonics of  $i_L(t)$  after the harmonic  $n_{sw}$  will be neglected since they are very small compared with the harmonic  $I_{L_{nsw}}$ . Therefore, the inductor current in the time domain can be approximated by the sum of  $I_L$  and  $I_{L_{nsw}}$ , as shown in Equation (15):

$$i_L(t) \approx I_L \sin(\omega t) + I_{L_{nsw}} \sin(\omega_{nsw} t) \tag{15}$$

According to Equation (15), it can be observed that the current ripple in the inductive L-filter is caused by the peak-to-peak amplitude of the current signal in the  $n_{sw}$  harmonic. Hence, the percentage of current ripple in the L-filter can be approximated by Equation (16):

$$\%r_{i_L} \approx \frac{(2I_{L_{nsw}})(100)}{I_L} \tag{16}$$

By substituting Equations (5) and (13) into Equation (16), the expression (17) is obtained.

$$\%r_{i_L} = \frac{100(m_{nsw})V_{dc}V_{grid}}{X_{L_{nsw}}P_{avg}} \tag{17}$$

Solving for  $L$  from Equation (14) and substituting Equation (17) results in Equation (18):

$$L = \frac{100(m_{nsw}V_{dc})V_{grid}}{\omega_{nsw}P_{avg}\%r_{i_L}} \tag{18}$$

### 2.4. Calculation of the DC-Level Bus Voltage

Once the inductor value is obtained, the analysis is performed to calculate the DC-level bus voltage. The inverter’s fundamental maximum output voltage  $V_1$  is related to the modulation index  $m$ , see Equation (19). The inverter output voltage is equal to the DC-level bus voltage [37,38].

$$V_1 = mV_{dc} \tag{19}$$

Combining Equations (19) and (14) and substituting the inductive reactance in Equation (2) results in Equation (20):

$$V_{dc} = \frac{|V_1|}{m} = \frac{\sqrt{V_{grid}^2 + (I_L\omega L)^2}}{m} \tag{20}$$

Substituting (5) and (18) in Equation (20) results in Equation (21):

$$V_{dc} = \frac{\sqrt{V_{grid}^2 + \frac{4000m_{nsw}^2V_{dc}^2\omega^2}{\%r_{i_L}^2\omega_{nsw}^2}}}{m} \tag{21}$$

Equation (10) is substituted and Equation (21) is divided into two parts, A and B, as shown in Equations (22) and (23):

$$A = V_{grid}^2 \tag{22}$$

$$B = \frac{30976\omega^2}{25\%r_{i_L}^2\omega_{nsw}^2} \tag{23}$$

Combining (22) and (23) in Equation (21) results in Equation (24):

$$V_{dc} = \frac{\sqrt{A + BV_{dc}^2}}{m} \tag{24}$$

Solving  $V_{dc}$  of Equation (24) results in Equation (25):

$$V_{dc} = \frac{\sqrt{A}}{\sqrt{m^2 - B}} \tag{25}$$

Substituting Equations (22) and (23) into Equation (25) results in Equation (26):

$$V_{dc} = \frac{\sqrt{V_{grid}^2}}{\sqrt{m^2 - \frac{30976\omega^2}{25\%r_{iL}^2\omega_{nsw}^2}}} \tag{26}$$

It is possible to calculate the DC bus level using Equation (26). The DC bus value must exceed the peak value of the grid voltage [39–42], even with ±5% variations. This equation is a function of the grid voltage ( $V_{grid}$ ), the ripple percentage ( $\%r_{iL}$ ), the modulation index ( $m$ ), and the angular switching frequency ( $\omega_{nsw}$ ). The average power of the DC–DC converter is approximately equal to the average output power supplied to the grid and the output power of the inverter without considering the switching losses of the MOSFETs; see Equation (4). Therefore, the average power delivered by the inverter can be expressed as a cosine function of the lag phase angle ( $\phi_{inv}$ ), and it is approximately equal to the average power delivered to the grid when the power factor at the connection point with the grid is unitary. This is shown in Equation (27).

$$P_{avg} = \frac{V_1 I_L}{2} \cos(\phi_{inv}) = \frac{V_{dc} I_L}{2m} \cos(\phi_{inv}) \tag{27}$$

Substituting (5) and solving for the angle phase caused by the L-filter results in Equation (28). For a modulation index, this is equal to 1.

$$\phi_{inv} = \cos^{-1}\left(\frac{V_{grid}}{V_{dc}}\right) \tag{28}$$

Equation (26) was solved for various values of the filter ripple current ( $\%r_{iL}$ ) and the specifications are shown in Table 1. Figure 6 shows the variation between  $V_{dc}$  and the current ripple. Figure 7 shows the different values of the L-filter for different  $P_{avg}$  and  $V_{dc}$  values when  $m$  is equal to 1.

**Table 1.** Specifications to obtain the DC-level bus voltage as a function of the L-filter ripple current.

Parameter	Symbol	Value
Maximum grid voltage	$V_{grid}$	180 V
Switching frequency of the SPWM	$f_{sw}$	15 kHz
Relationship between the maximum output voltage at the harmonic $n_{sw}$ ( $V_{nsw}$ ) and the DC-level bus voltage ( $V_{dc}$ ) <sup>1</sup>	$m_{nsw}$	0.176
Percentage of current ripple in the filter L	$\%r_{iL}$	0.08% to 0.6%

<sup>1</sup> Corresponding values for a SPWM unipolar modulation with modulation index = 1.

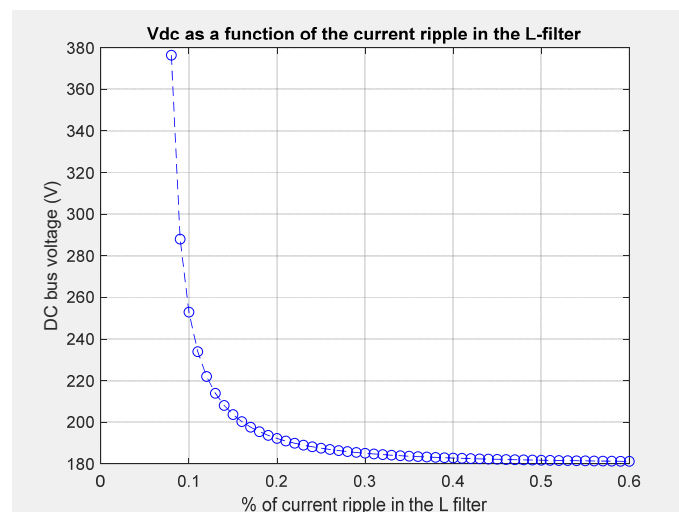


**Figure 6.**  $V_{dc}$  as a function of the current ripple in the L-filter.

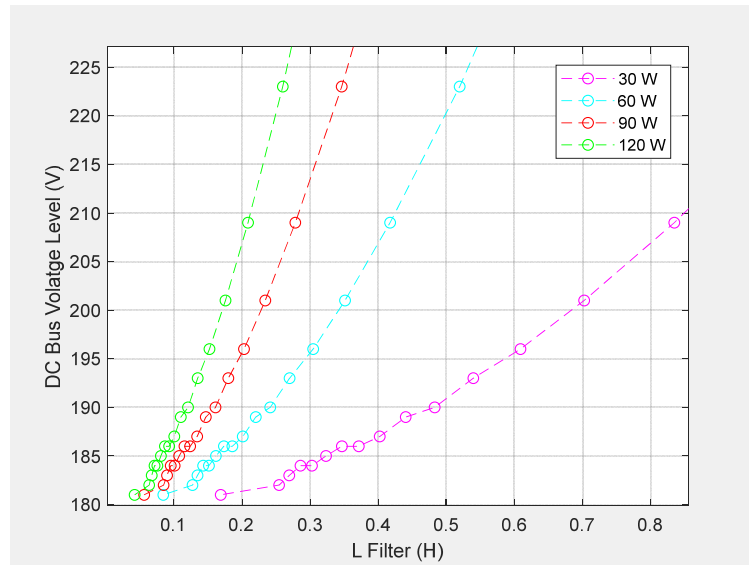


**Figure 7.** L-filter and DC bus voltage levels at different average power levels.

2.5. Evaluation of the Current Total Harmonic Distortion ( $THD_i$ )

The  $THD_i$  in the L-filter can be calculated with Equation (29)

$$\%THD_i = \frac{\sqrt{I_{nsw1}^2 + I_{nsw2}^2 + I_{nsw3}^2 + \dots + I_{nsw_n}^2}}{I_L} \quad (29)$$

where  $I_{nsw1}, I_{nsw2}, I_{nsw3}$  up to  $I_{nsw_n}$  are the main harmonics that are multiples of the harmonic  $n_{sw}$ . These harmonics are found at frequencies of 30.06 kHz, 60.06 kHz, 90.06 kHz, and so on. To calculate the values of the currents in these harmonics, we use Equation (30).

$$I_{nsw_n} = \frac{V_{nsw_n}}{\omega_{nsw}L} \quad (30)$$

where  $I_{nsw_n}$  is the current for any harmonic,  $V_{nsw_n}$  is the inverter voltage for any harmonic, and  $\omega_{nsw_n}$  is the angular frequency for any harmonic. Using Equations (7) and (30) and substituting into Equation (29) gives the  $THD$  result for the L-filter current, as shown in Equation (31).

$$\%THD_i = 0.23\% \quad (31)$$

The  $THD$  is very low due to the high switching frequency  $f_{sw} = 15$  kHz.

3. Link Capacitor Analysis

The theoretical analysis to assess the link capacitor’s effect on the DC-level bus voltage is shown below. According to experimental and simulation results, the voltage on the link capacitor as a function of time could be approximated to one expression with two components: one DC component and one AC component. The AC component is the ripple voltage in the capacitor, as shown in the Equation (32):

$$v_{C_{link}} = V_{dc} + \frac{\Delta V_{dc}}{2} \sin(2\omega t + \phi_{inv}) \quad (32)$$

where  $V_{dc}$  is the DC bus voltage,  $\Delta V_{dc}$  is the peak-to-peak voltage of the ripple on the link capacitor, which oscillates at twice the grid frequency ( $2\omega t$ ), and  $\phi_{inv}$  is the phase angle evaluated in (3). The DC bus level can be defined by Equation (33):

$$V_{dc} = V_{max} - \left( \frac{\Delta v_{dc}}{2} \right) \quad (33)$$

where  $V_{max}$  is the maximum voltage of the ripple on the link capacitor. The percentage of the voltage ripple on the link capacitor is calculated with Equation (34):

$$\% \Delta r_{vdc} = \frac{\Delta V_{dc}(100)}{V_{dc}} \tag{34}$$

The expression of current in a capacitor is (35):

$$i_{C_{link}} = C_{link} \frac{dv_{C_{link}}}{dt} \tag{35}$$

where  $i_{C_{link}}$  is the current in the link capacitor. Substituting (32) and into Equation (35) gives (36):

$$i_{C_{link}} = \omega C_{link} \Delta v_{dc} \cos(2\omega t + \phi_{inv}) \tag{36}$$

Kirchhoff’s current law is applied to the node where the link capacitor is located (see Figure 7). When the inverter returns energy, the capacitor is charged, and when the inverter demands energy, the capacitor is discharged. In Figure 8, the red signal is the output current of the DC–DC converter, the purple signal is the current at the inverter input, and the blue signal is the current in the link capacitor. The red ellipses show the energy return from the L-filter to the DC bus and the link capacitor. Considering Figure 9, Kirchhoff’s current law at the node of the link capacitor is given in Equation (37).

$$i_{dc} + i_{C_{link}} - i_{inv} = 0 \tag{37}$$

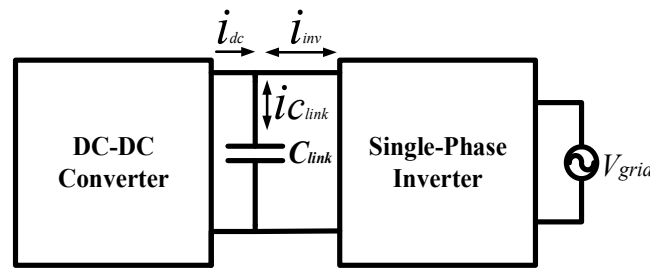


Figure 8. Currents in the link capacitor.

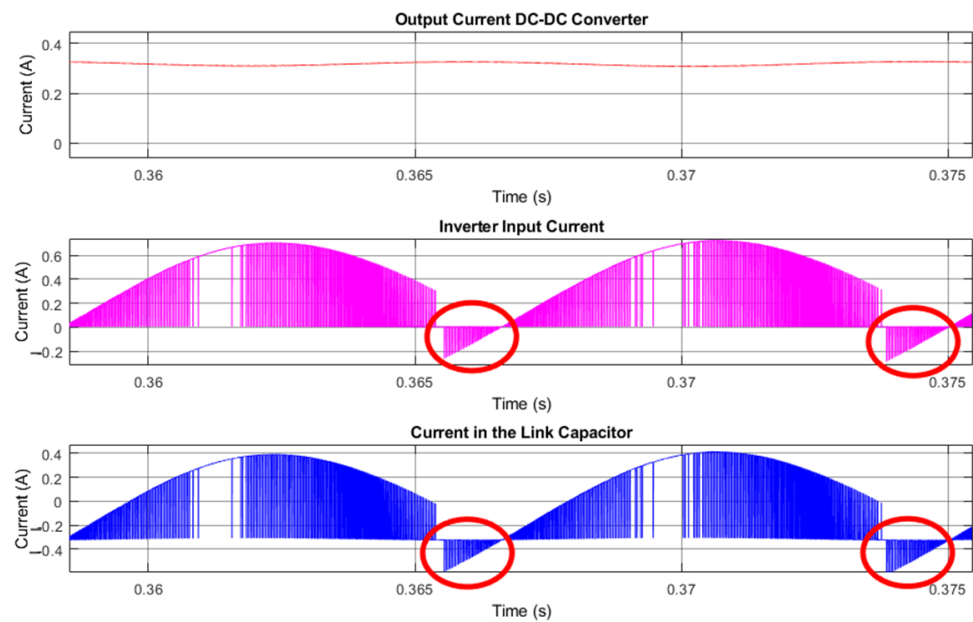


Figure 9. Link capacitor node currents and returned power (red ellipses).

Equation (36) is substituted into (37) and the maximum values are taken. Solving for  $i_{C_{link}}$  results in (38):

$$I_{C_{link}max} = I_{invmax} - I_{dcmax} = \omega C_{link} \Delta_{vdc} \tag{38}$$

By subtracting  $C_{link}$  from Equation (38), considering that the magnitude of the current  $I_{invmax}$  is the same as  $I_L$  because the losses in the inverter are minimized, the link capacitor can be calculated with Equation (39):

$$C_{link} = \frac{I_{Lmax} - (I_{dc})}{\omega \Delta_{vdc}} = \frac{\left(\frac{2P_{avg}}{V_{grid}}\right) - \left(\frac{P_{avg}}{V_{dc}}\right)}{\omega \Delta_{vdc}} \tag{39}$$

Combining Equation (28) with Equation (39) results in (40):

$$C_{link} = \frac{\left(\frac{2P_{avg}}{V_{grid}}\right) - \left(\frac{P_{avg}}{\frac{V_{grid}}{\cos(\phi_{inv})}}\right)}{\omega \Delta_{vdc}} \tag{40}$$

Simplifying Equation (40) results in (41):

$$C_{link} = \frac{P_{avg}(2 - \cos(\phi_{inv}))}{V_{grid}\omega \Delta_{vdc}} \tag{41}$$

Combining (34) with (41) gives Equation (42):

$$C_{link} = \frac{100P_{avg}(2 - \cos(\phi_{inv})) \cos(\phi_{inv})}{V_{grid}^2 \omega \% \Delta r_{vdc}} \tag{42}$$

In Equation (42), the capacitor value is a function of the energy returned by the L-filter caused by the phase-shift angle  $\phi_{inv}$ . Figure 10 shows the values for the link capacitor at different power and ripple percentages.

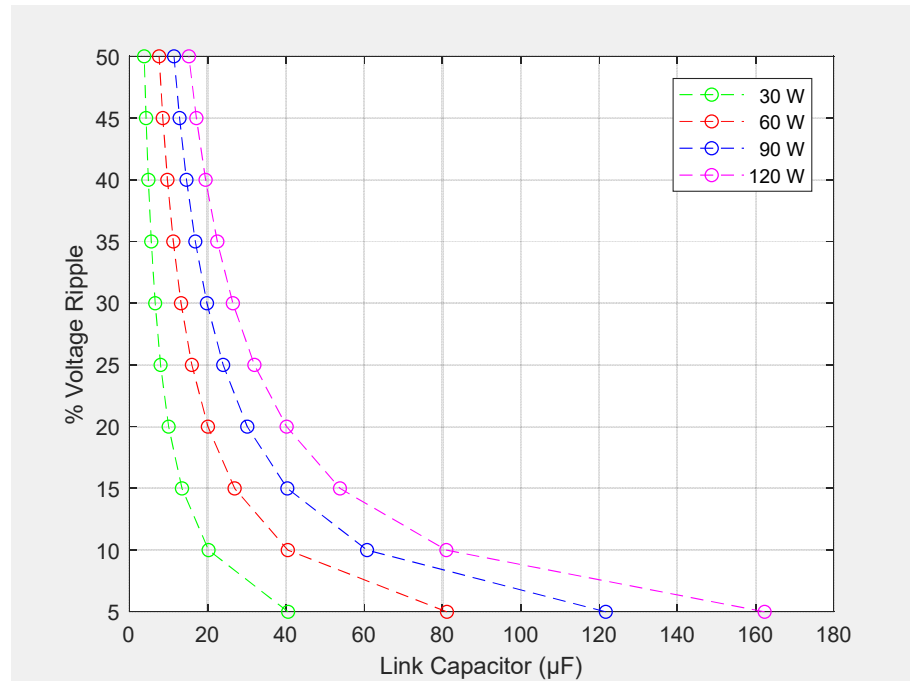


Figure 10. Link capacitor and % voltage ripple at different average power ratings.

#### 4. Design Methodology

To validate the above equations, a step-by-step design methodology is proposed in this work. The design specifications are based on the information shown in Table 1. Table 2 shows the general design specifications. The general specifications are proposed for the

application of a microinverter connected to the grid, which is why the average power is low, the  $\beta$  ratio is high to obtain a low %THDi, and the percentage of voltage ripple is small.

**Table 2.** General design specifications.

Parameter	Symbol	Value
Average power	$P_{avg}$	60 W
Grid frequency	$f_g$	60 Hz
Frequency ratio	$\beta$	250
Voltage ripple percentage	$\% \Delta r_{vdc}$	15%
Angular grid frequency	$\omega$	$120 \pi$ rad/s

Given the conditions in Table 2, Table 3 shows the DC–DC converter design specifications. The input voltage of the DC–DC converter comes from photovoltaic panels, the switching frequency is a typical value in DC–DC converters, and the current and voltage ripples are proposed to be small.

**Table 3.** DC–DC converter design specifications.

Parameter	Symbol	Value
Voltage of PV panels	$V_{PV}$	30.3 V
Switching frequency of the DC–DC converter	$f_s$	100 kHz
Current ripple on inductor $L_1$	$\Delta i_{L1}$	0.3 A 4.5% of $I_{PV}$
Current ripple on inductor $L_2$	$\Delta i_{L2}$	0.066 A 10% of $I_{dc}$
Voltage ripple on capacitor $C_{1p}$	$\Delta v_{C1p}$	1.5 V $\approx$ 5% of $V_{PV}$
Voltage ripple on capacitor $C_{1s}$	$\Delta v_{C1s}$	10 V $\approx$ 5% of $V_{dc}$
Transformer turns ratio	$n_p/n_s$	1/4

Table 4 shows the step-by-step design methodology for the inverter and L-filter. The only value proposed is  $V_{dc}$  and the others are obtained with the equations shown in the tables.

**Table 4.** Proposed design methodology for the inverter and L-filter.

Step	Parameter	Symbol	Equation	Value
1	DC bus voltage	$V_{dc}$	Proposed Value	209 V
2	Offset angle	$\phi_{inv}$	$\phi_{inv} = \cos^{-1} \left( \frac{V_{grid}}{V_{dc}} \right)$	0.53 rad/s
3	Link capacitor	$C_{link}$	$C_{link} = \frac{100P_{avg}(2 - \cos(\phi_{inv})) \cos(\phi_{inv})}{V_{grid}^2 \omega \% \Delta r_{vdc}}$	34.7 $\mu$ F
4	Current ripple percentage	$\% r_{iL}$	See Figure 5	0.14%
5	L-filter	$L$	$L = \frac{100(m_{nsw} V_{dc}) V_{grid}}{\omega_{nsw} P_{avg} \% r_{iL}}$	417 mH
6	Percentage harmonic current distortion	$\% THD_i$	$\% THD_{iL} = \frac{\sqrt{I_{nsw1}^2 + \dots + I_{nswn}^2}}{I_L} (100)$	0.23%
7	Filter inductor current	$I_L$	$I_L = \frac{2P_{avg}}{V_{grid}}$	0.663 A
8	Inductive reactance of the filter inductor	$X_L$	$X_L = \omega L$	157.2 $\Omega$

Table 5 shows the step-by-step design methodology for the DC–DC converter; this methodology is based on Table 3.

The magnetic design of the transformer is carried out using the geometric constant method ( $K_{gfe}$ ) applied to transformers [43]. Table 6 shows the parameters obtained for the construction of the transformer, where the number of wires indicates the thickness of the transformer windings. The number of turns is determined with reference to the reel (ETD29).

**Table 5.** Design methodology for the DC–DC converter.

Step	Parameter	Symbol	Equation	Value
9	Duty cycle	$D$	Proposed Value	63.40%
10	DC–DC converter gain	$M$	$D = \left( \frac{n_p V_{dc}}{n_s V_{in} + n_p V_{dc}} \right) (100\%)$	6.93
11	Switching period of the DC–DC converter	$T_s$	$T_s = \frac{1}{f_s}$	10 $\mu$ S
12	DC–DC converter on-time	$t_{on}$	$t_{on} = DT_s$	6.34 $\mu$ S
13	DC–DC converter off-time	$t_{off}$	$t_{off} = (1 - D)T_s$	3.66 $\mu$ S
14	Inductor 1	$L_1$	$L_1 = \frac{V_{in} DT_s}{\Delta I_{L1}(t_{on})}$	0.640 mH
15	Inductor 2	$L_2$	$L_2 = \frac{V_{dc}(1-D)T_s}{\Delta I_{L2}(t_{off})}$	3.24 mH
16	Capacitor $C_{1p}$	$C_{1p}$	$C_{1p} = \frac{n_s}{n_p} \frac{I_{dc} D}{\Delta V_{C_{1p}} f_s}$	4.915 $\mu$ F
17	Capacitor $C_{1s}$	$C_{1s}$	$C_{1s} = \frac{I_{dc} D}{\Delta V_{C_{1s}} f_s}$	0.1843 $\mu$ F

**Table 6.** Magnetic transformer design.

Number of Primary Winding Turns	Number of Primary Winding Wires	Number of Secondary Windings Turns	Number of Secondary Winding Wires	Caliber	Reel/Material
10	35	40	13	AWG 30	ETD29/3C90

### 5. Simulation Results

To verify the performance of the design, an open-loop simulation was performed with Simulink software. The schematic is shown in Figure 11, where the DC–DC converter is connected to the inverter, which is controlled by the phase-shift angle  $\phi_{inv}$  and the unipolar SPWM modulation technique. The inverter is connected to an L-filter and connected to the grid. The schematic is shown in Figure 11.

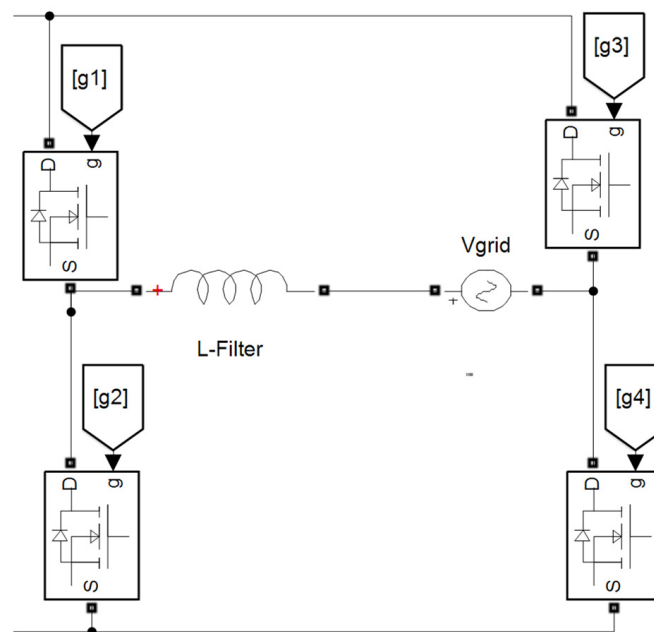


**Figure 11.** Single-phase inverter with L-filter connected to the grid.

The isolated Cuk converter is shown in Figure 12.

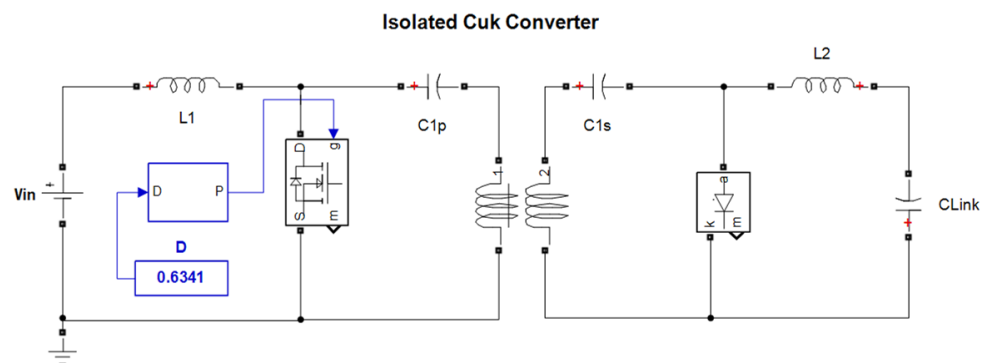


Figure 12. Isolated Cuk converter.

Figure 13 shows the simulation results for voltage, current, instantaneous power, and average power in the grid. The theoretical value of the grid current is 0.66 A, and the value obtained in simulation is 0.6775, giving an error of 1.5%. The theoretical value of the maximum instantaneous power is 120 W, and the measured value is 121.8 W, giving an error of 1.5%. The calculated average power is 60 W, and the measured value is 60.9, which is a 1.5% error. The current and voltage are at a fundamental frequency of 60 Hz, and the instantaneous power is at a frequency of 120 Hz.

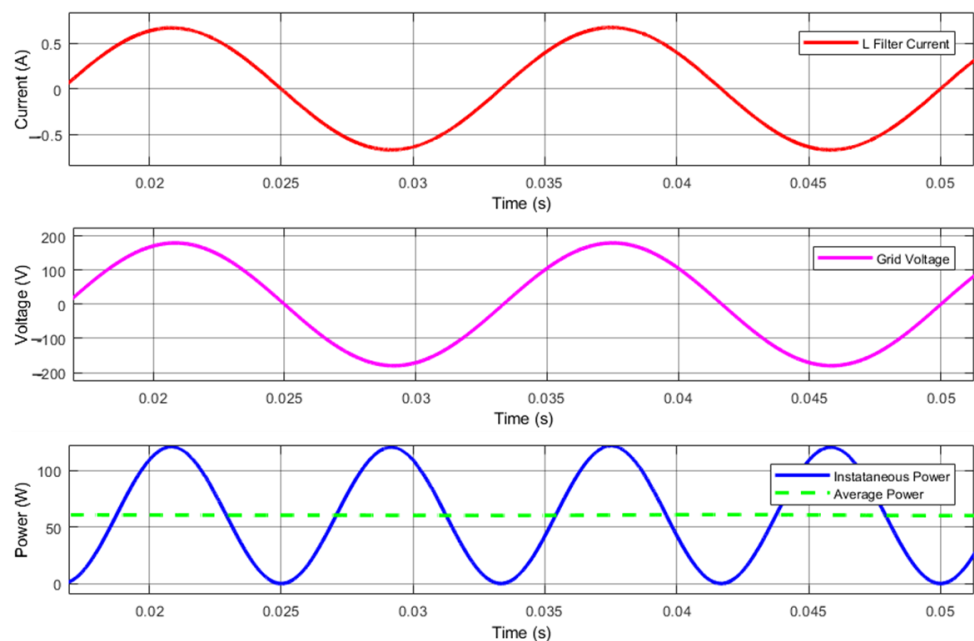


Figure 13. Simulation results: current (upper trace), voltage (middle trace), and instantaneous power injected into the main grid (lower trace).

To obtain the percentage of the magnitude in the harmonic  $n_{sw}$  shown in Figure 14, Equation (16) must be divided by 2 since this equation expresses the percentage of ripple. However, in the FFT shown in Figure 13, the percentage is a function of the fundamental peak magnitude. The current ripple percentage in the L-filter was proposed to be 0.14%, so when substituting this value in (43), we obtain a percentage of 0.07%, which is what is shown in the FFT.

$$\%I_{L_{nsw}} = \frac{\%r_{iL}}{2} = 0.07\% \tag{43}$$

The value calculated using (43) is shown in Figure 14. This percentage appears for harmonics  $(2\beta - 1)$  and  $(2\beta + 1)$ , while for harmonics  $(2\beta - 2)$  and  $(2\beta + 2)$ , it is slightly higher than the proposed value. Figure 15 shows the grid voltage at a frequency of 60 Hz and the voltage ripple on the DC bus at a frequency of 120 Hz. It is observed that the ripple

is 29 V, which corresponds to a percentage ripple of  $\% \Delta r_{vdc} = 13.7\%$ . The proposed value was 15%, so the error was 8.6%.

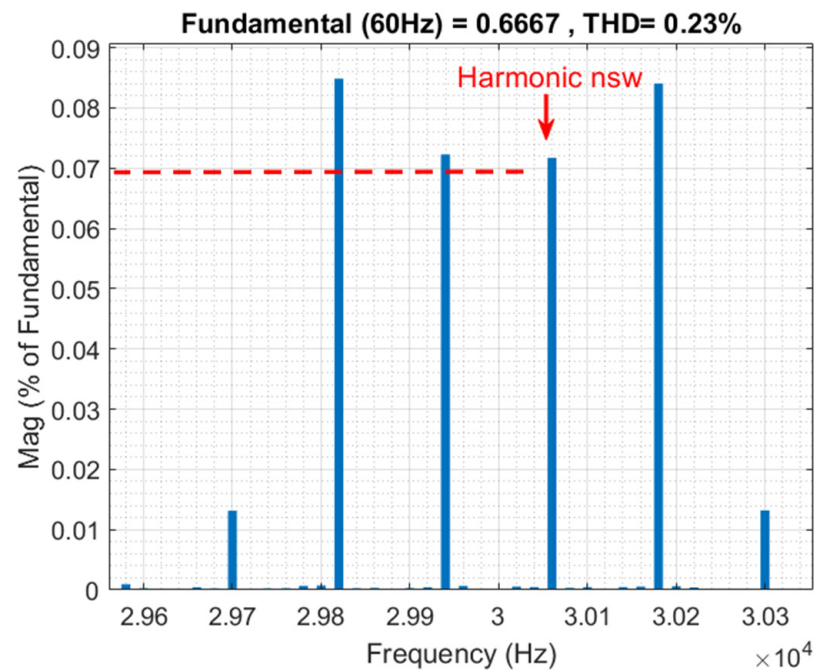


Figure 14. FFT in the current L-filter.

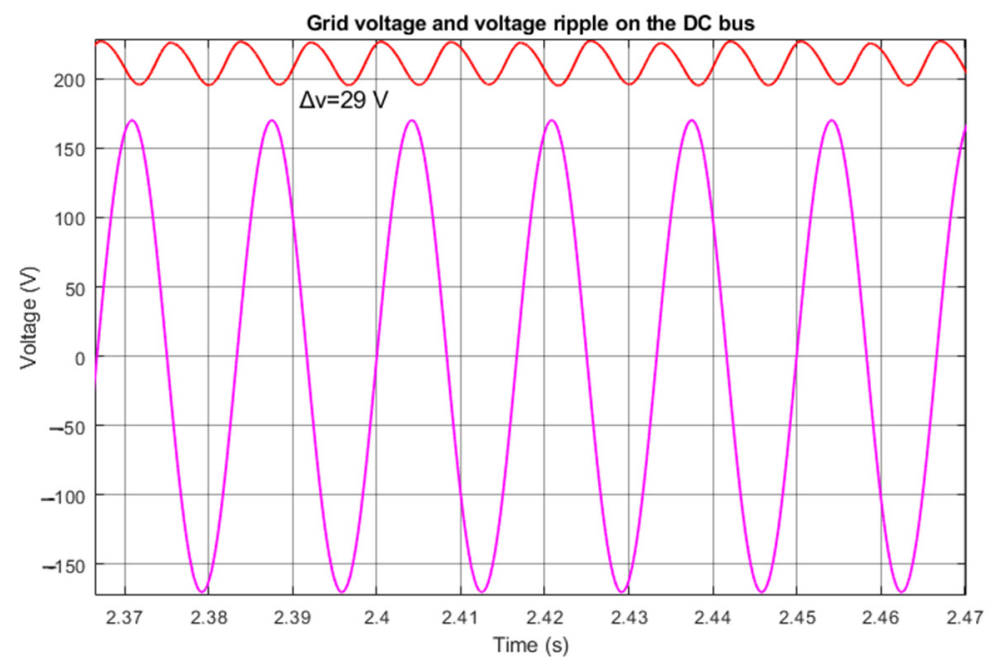


Figure 15. Grid voltage and voltage ripple on the DC bus.

An analysis was performed for a power of 1 kW, obtaining an L-filter of 25 mH and a peak current in the L-filter of 5.55 A. As a result, an average power of 985.1 W was obtained, and the proposed value was 1000 W with an error percentage of 1.5%, corresponding to an efficiency of 98%. This is shown in Figure 16.

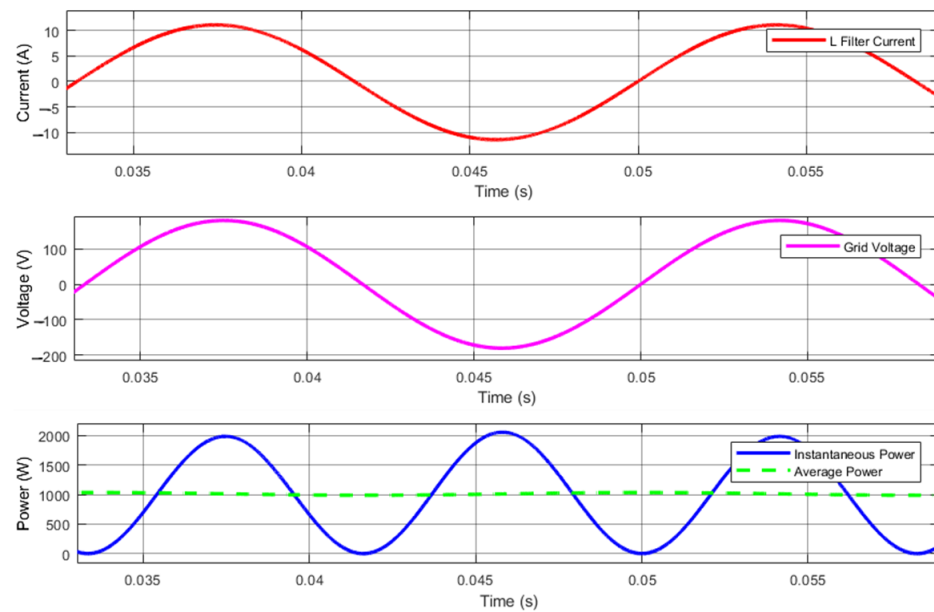


Figure 16. Simulation at an average power of 1 kW.

### 6. Experimental Results

A prototype is implemented experimentally to validate the design methodology and calculations performed. The values obtained from Tables 2–5 were used. The devices used are shown in Table 7. Figure 17 shows the voltage on the grid and the ripple voltage on the link capacitor. The grid voltage is the magenta signal. The grid voltage presents a maximum voltage of 176 V measured, and the theoretical value is 180 V, which gives an error of 2.27%. The ripple voltage on the link capacitor is the navy-blue signal with a peak-to-peak value of 29 Vpp measured, and the proposed theoretical value in percent was 15%, or 31.35 Vpp. This gives a percentage error of 8.1%. The prototype is shown in Figures 18 and 19.

Table 7. Devices used in the prototype.

Device	Description	Model
PWM controller	PWM controller of the DC–DC converter	UC3823
Power diode	Diode of the DC–DC converter	U15A60
Power MOSFET	DC–DC converter power MOSFET	CMF20120
Power transistors	Full-bridge power inverter	IRAM10UP60A

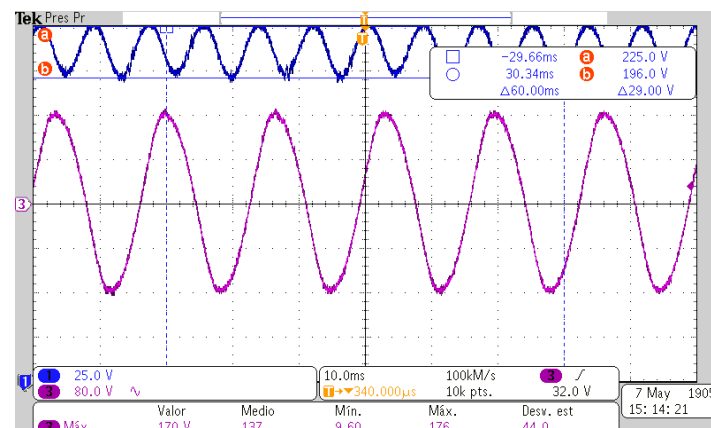
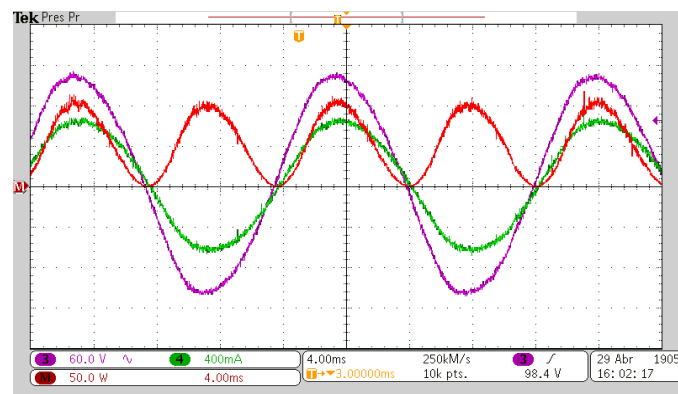
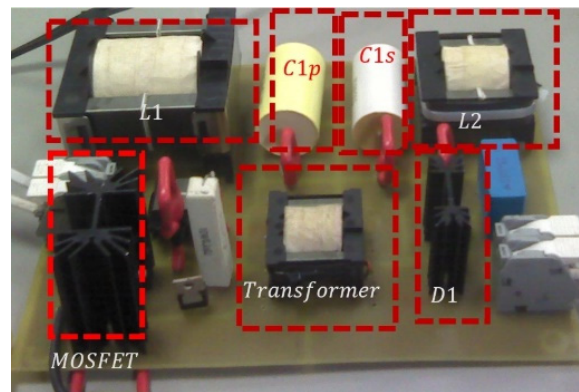


Figure 17. Grid voltage (purple signal) and link capacitor voltage ripple (navy blue signal).



**Figure 18.** Grid voltage (purple signal), current injected into the grid (green signal), and instantaneous power at the point of connection (red signal).



**Figure 19.** Implemented prototype of the isolated Cuk converter.

Figure 18 shows the grid voltage (purple color signal), the instantaneous power (red color signal), with an average measured value of 56.4 W, and the proposed theoretical value of 60 W, which gives an error of 6.3%. The current injected into the grid (green color signal) had a measured value of 640 mA, and the proposed theoretical value was 663 mA, which gives an error of 3.59%. Dividing the measured output power by the theoretical value results in 0.94. Therefore, the efficiency of the DC–DC and DC–AC converters is 94%.

Figure 19 shows the isolated Cuk converter used. The components are framed in red rectangles. Figure 20 shows the complete bridge inverter module occupied.

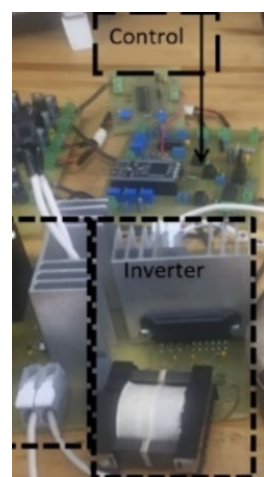


**Figure 20.** Implemented DC–AC converter.

## 7. Discussion

Table 8 shows two comparisons. The first is between the measured voltage ripple values and the proposed voltage ripple percentage values. The link capacitor is calculated using Equation (42). With this equation, an error of less than 10% is achieved. The second comparison is made with respect to Equation (44) published in several articles [9,20,44], and without using a control loop for DC bus voltage. In (44), the energy returned by the inverter output filters is not considered.

$$C_{link} = \frac{P_{avg}}{\omega V_{dc} \Delta V_{dc}} \quad (44)$$

**Table 8.** Comparison between Equations (42) and (44).

Calculated Values with (42) and Measured Values				Calculated Values with (44) and Measured Values		
% $\Delta r_{vdc}$	Measured Value ( $\Delta V_{dc}$ )	$C_{link}$	% Error	Measured Value ( $\Delta V_{dc}$ )	$C_{link}$	% Error
0.5%	1.008 V	0.97 mF	±0.5%	1.20 V	0.79 mF	±16.3%
1%	2.1 V	4.8 $\mu$ F	±4.5%	2.41 V	3.96 $\mu$ F	±16.9%
5%	9.52 V	97.22 $\mu$ F	±5.2%	11.64 V	79.26 $\mu$ F	±13.9%
10%	18.97 V	48.61 $\mu$ F	±5.6%	23.84 V	39.63 $\mu$ F	±15.9%

## 8. Conclusions

In this work, a mathematical analysis of the energy returned by an L-filter and sent to the link capacitor in single-phase photovoltaic systems connected to the grid has been presented. A new equation has been proposed for the calculation of the link capacitor as a function of the energy returned by an L-filter, which presents an error of less than 6%, with a total system efficiency of 94%. A new design method has been proposed for an L-filter as well as for the DC bus as a function of the percentage of ripple current injected into the grid without the use of Bode diagrams. The proposed method presents an error of less than 4% compared to the proposed current value. These are the article's main contributions. Everything presented in this article can be applied to the design of microinverters for photovoltaic applications that are interconnected to the grid through an L-filter. The limitation of this work is that it only applies to a specific type of filter, the L-filter, and only for single-phase systems connected to the grid; it cannot be used for a three-phase system.

**Author Contributions:** Conceptualization, H.A.-P., M.P.-S., J.D.M.-A. and A.C.-S.; methodology, M.P.-S., J.D.M.-A., A.C.-S. and H.A.-P.; software, H.A.-P., A.C.-S., O.R.-B. and H.A.-P.; validation, M.P.-S., J.D.M.-A., O.R.-B. and A.C.-S.; formal analysis, H.A.-P., M.P.-S., A.C.-S. and H.A.-P.; investigation, H.A.-P., M.P.-S., J.D.M.-A. and A.C.-S.; resources, H.A.-P., O.R.-B. and H.A.-P.; data curation, J.D.M.-A., A.C.-S., O.R.-B. and H.A.-P.; writing—original draft preparation, H.A.-P., J.D.M.-A., H.A.-P. and A.C.-S.; writing—review and editing, H.A.-P., M.P.-S., J.D.M.-A., A.C.-S. and O.R.-B.; visualization, A.C.-S., O.R.-B. and H.A.-P.; supervision, M.P.-S., J.D.M.-A., O.R.-B. and H.A.-P.; project administration, M.P.-S. and O.R.-B.; funding acquisition and, M.P.-S., H.A.-P. and O.R.-B. All authors have read and agreed to the published version of the manuscript.

**Funding:** This research received no external funding.

**Conflicts of Interest:** The authors declare no conflict of interest.

## References

1. Feron, S. Sustainability of Off-Grid Photovoltaic Systems for Rural Electrification in Developing Countries: A Review. *Sustainability* **2016**, *8*, 1326.
2. Zeb, K.; Khan, I.; Uddin, W.; Khan, M.A.; Sathishkumar, P.; Busarello, T.D.C.; Ahmad, I.; Kim, H.J. A Review on Recent Advances and Future Trends of Transformerless Inverter Structures for Single-Phase Grid-Connected Photovoltaic Systems. *Energies* **2018**, *11*, 1968. [[CrossRef](#)]

3. Zahedi, R.; Ranjbaran, P.; Gharehpetian, G.B.; Mohammadi, F.; Ahmadiyahangar, R. Cleaning of Floating Photovoltaic Systems: A Critical Review on Approaches from Technical and Economic Perspectives. *Energies* **2021**, *14*, 2018.
4. Kim, J.; Rabelo, M.; Padi, S.P.; Yousuf, H.; Cho, E.-C.; Yi, J. A Review of the Degradation of Photovoltaic Modules for Life Expectancy. *Energies* **2021**, *14*, 4278. [[CrossRef](#)]
5. Sangwongwanich, A.; Yang, Y.; Sera, D.; Blaabjerg, F. Mission profile-oriented control for reliability and lifetime of photovoltaic inverters. *IEEE Trans. Ind. Appl.* **2019**, *56*, 601–610. [[CrossRef](#)]
6. Raghavendra, K.V.G.; Zeb, K.; Muthusamy, A.; Krishna, T.N.V.; Prabhudeva Kumar, S.V.S.V.; Kim, D.-H.; Kim, M.-S.; Cho, H.-G.; Kim, H.-J. A Comprehensive Review of DC–DC Converter Topologies and Modulation Strategies with Recent Advances in Solar Photovoltaic Systems. *Electronics* **2020**, *9*, 31.
7. Jamatia, A.; Gautam, V.; Sensarma, P. Power Decoupling for Single-Phase PV System Using Ćuk Derived Microinverter. *IEEE Trans. Ind. Appl.* **2018**, *54*, 3586–3595. [[CrossRef](#)]
8. Roy, J.; Xia, Y.; Ayyanar, R. Half-Bridge Voltage Swing Inverter with Active Power Decoupling for Single-Phase PV Systems Supporting Wide Power Factor Range. *IEEE Trans. Power Electron.* **2018**, *34*, 7450–7461. [[CrossRef](#)]
9. Rezaei, M.H.; Akhbari, M. Power decoupling capability with PR controller for Micro-Inverter applications. *Int. J. Electr. Power Energy Syst.* **2021**, *136*, 107607.
10. Rodríguez-Benítez, O.; Ponce-Silva, M.; Aquí-Tapia, J.A.; Rodríguez-Benítez, M.; Lozoya-Ponce, R.E.; Adamas-Pérez, H. Active Power-Decoupling Methods for Photovoltaic-Connected Applications: An Overview. *Processes* **2023**, *11*, 1808.
11. Watanabe, H.; Itoh, J.-I.; Koike, N.; Nagai, S. PV Micro-Inverter Topology Using LLC Resonant Converter. *Energies* **2019**, *12*, 3106. [[CrossRef](#)]
12. Musarrat, M.N.; Islam, M.R.; Muttaqi, K.M.; Sutanto, D. Shunt active DC filter to reduce the DC-link ripple current caused by power converters to improve the lifetime of aluminum electrolytic capacitors. *IEEE Trans. Ind. Appl.* **2021**, *57*, 4306–4315. [[CrossRef](#)]
13. Alcaide, A.M.; Ko, Y.; Andresen, M.; Leon, J.I.; Vazquez, S.; Monopoli, V.G.; Buticchi, G.; Liserre, M.; Franquelo, L.G. Capacitor Lifetime Extension of Interleaved DC–DC Converters for Multistring PV Systems. *IEEE Trans. Ind. Electron.* **2022**, *70*, 4854–4864. [[CrossRef](#)]
14. Ramos-Paja, C.A.; Danilo-Montoya, O.; Grisales-Noreña, L.F. Photovoltaic System for Microinverter Applications Based on a Non-Electrolytic-Capacitor Boost Converter and a Sliding-Mode Controller. *Electronics* **2022**, *11*, 2923.
15. Qi, W.; Wang, M.; Li, S. Transformerless Three-Level Flying-Capacitor Step-Up PV Micro-Inverter Without Electrolytic Capacitors. *IEEE J. Emerg. Sel. Top. Circuits Syst.* **2020**, *11*, 49–58. [[CrossRef](#)]
16. Qi, W.; Li, S.; Tan, S.-C.; Hui, S.Y. A Single-Phase Three-Level Flying-Capacitor PFC Rectifier Without Electrolytic Capacitors. *IEEE Trans. Power Electron.* **2018**, *34*, 6411–6424. [[CrossRef](#)]
17. Zhao, N.; Wang, G.; Xu, D.; Zhu, L.; Zhang, G.; Huo, J. Inverter Power Control Based on DC-Link Voltage Regulation for IPMSM Drives Without Electrolytic Capacitors. *IEEE Trans. Power Electron.* **2017**, *33*, 558–571. [[CrossRef](#)]
18. Marcos-Pastor, A.; Vidal-Idiarte, E.; Cid-Pastor, A.; Martínez-Salamero, L. Minimum DC-Link Capacitance for Single-Phase Applications with Power Factor Correction. *IEEE Trans. Ind. Electron.* **2019**, *67*, 5204–5208. [[CrossRef](#)]
19. Sangwongwanich, A.; Shen, Y.; Chub, A.; Liivik, E.; Vinnikov, D.; Wang, H.; Blaabjerg, F. Mission profile-based accelerated testing of DC-link capacitors in photovoltaic inverters. In Proceedings of the 2019 IEEE Applied Power Electronics Conference and Exposition (APEC), Anaheim, CA, USA, 17–21 March 2019; pp. 2833–2840.
20. Sangwongwanich, A.; Shen, Y.; Chub, A.; Liivik, E.; Vinnikov, D.; Wang, H.; Blaabjerg, F. Design for Accelerated Testing of DC-Link Capacitors in Photovoltaic Inverters Based on Mission Profiles. *IEEE Trans. Ind. Appl.* **2021**, *57*, 741–753.
21. Li, J.; Song, Z.; Wang, X.; Wang, Y.; Jia, Y. A novel offshore wind farm typhoon wind speed prediction model based on PSO–Bi-LSTM improved by VMD. *Energy* **2022**, *251*, 123848.
22. Li, L.-L.; Liu, Z.-F.; Tseng, M.-L.; Zheng, S.-J.; Lim, M.K. Improved tunicate swarm algorithm: Solving the dynamic economic emission dispatch problems. *Appl. Soft Comput.* **2021**, *108*, 107504.
23. Liu, Z.; Ware, T. Capturing spatial influence in wind prediction with a graph convolutional neural network. *Front. Environ. Sci.* **2022**, *10*, 25.
24. Liu, Z.-F.; Li, L.-L.; Liu, Y.-W.; Liu, J.-Q.; Li, H.-Y.; Shen, Q. Dynamic economic emission dispatch considering renewable energy generation: A novel multi-objective optimization approach. *Energy* **2021**, *235*, 121407.
25. Benyoucef, A.; Kara, K.; Chouder, A.; Silvestre, S. Prediction-based Deadbeat Control for Grid-connected Inverter with L-filter and LCL-filter. *Electr. Power Compon. Syst.* **2014**, *42*, 1266–1277. [[CrossRef](#)]
26. Scoltock, J.; Geyer, T.; Madawala, U. Model Predictive Direct Current Control for a grid-connected converter: LCL-filter versus L-filter. In Proceedings of the 2013 IEEE International Conference on Industrial Technology (ICIT), Cape Town, South Africa, 25–28 February 2013; pp. 576–581.
27. Yagnik, U.P.; Solanki, M.D. Comparison of L, LC & LCL filter for grid connected converter. In Proceedings of the 2017 International Conference on Trends in Electronics and Informatics (ICEI), Tirunelveli, India, 11–12 May 2017; pp. 455–458.
28. Cha, H.; Vu, T.-K. Comparative analysis of low-pass output filter for single-phase grid-connected Photovoltaic inverter. In Proceedings of the 2010 Twenty-Fifth Annual IEEE Applied Power Electronics Conference and Exposition (APEC), Palm Springs, CA, USA, 21–25 February 2010; pp. 1659–1665.

29. Renzhong, X.; Lie, X.; Junjun, Z.; Jie, D. Design and research on the LCL filter in three-phase PV grid-connected inverters. *Int. J. Comput. Electr. Eng.* **2013**, *5*, 322.
30. Costa, J.S.; Lunardi, A.; Ribeiro, P.C.; Da Silva, I.B.; Fernandes, D.A.; Filho, A.J.S. Performance-Based Tuning for a Model Predictive Direct Power Control in a Grid-Tied Converter With L-Filter. *IEEE Access* **2023**, *11*, 8017–8028.
31. Zhang, Q.; Tang, Y.; Hou, L.; Deng, F.; An, S.; Sun, X. An Active High Frequency Damping Scheme for the Current Control of L Filter-Based Grid-Connected Inverter. *IEEE Access* **2019**, *7*, 171738–171751. [[CrossRef](#)]
32. Wei, X.; Xiao, L.; Yao, Z.; Gong, C. Design of LCL filter for wind power inverter. In Proceedings of the 2010 World Non-Grid-Connected Wind Power and Energy Conference, Nanjing, China, 5–7 November 2010; pp. 1–6.
33. Jiao, N.; Wang, S.; Liu, T.; Wang, Y.; Chen, Z. Harmonic Quantitative Analysis for Dead-Time Effects in SPWM Inverters. *IEEE Access* **2019**, *7*, 43143–43152. [[CrossRef](#)]
34. Asefi, M.; Nazarzadeh, J. Integral-series Fourier analysis of chaotic PWM patterns for common mode voltage stresses. *IET Power Electron.* **2018**, *11*, 1591–1602. [[CrossRef](#)]
35. Hren, A.; Mihalič, F. An Improved SPWM-Based Control with Over-Modulation Strategy of the Third Harmonic Elimination for a Single-Phase Inverter. *Energies* **2018**, *11*, 881. [[CrossRef](#)]
36. Ray, R.N.; Chatterjee, D.; Goswami, S.K. An application of PSO technique for harmonic elimination in a PWM inverter. *Appl. Soft Comput.* **2009**, *9*, 1315–1320. [[CrossRef](#)]
37. Prabakaran, N.; Palanisamy, K. Comparative analysis of symmetric and asymmetric reduced switch MLI topologies using unipolar pulse width modulation strategies. *IET Power Electron.* **2016**, *9*, 2808–2823. [[CrossRef](#)]
38. Sarker, R.; Datta, A.; Debnath, S. FPGA-based variable modulation-indexed-SPWM generator architecture for constant-output-voltage inverter applications. *Microprocess. Microsyst.* **2020**, *77*, 103123. [[CrossRef](#)]
39. Huang, K.-P.; Wang, Y.; Wai, R.-J. Design of Power Decoupling Strategy for Single-Phase Grid-Connected Inverter Under Nonideal Power Grid. *IEEE Trans. Power Electron.* **2018**, *34*, 2938–2955. [[CrossRef](#)]
40. Shinjo, F.; Wada, K.; Shimizu, T. A single-phase grid-connected inverter with a power decoupling function. In Proceedings of the 2007 IEEE Power Electronics Specialists Conference, Sapporo, Japan, 21–24 June 2010; pp. 1245–1249.
41. Rahim, N.A.; Chaniago, K.; Selvaraj, J. Single-Phase Seven-Level Grid-Connected Inverter for Photovoltaic System. *IEEE Trans. Ind. Electron.* **2010**, *58*, 2435–2443.
42. Zhang, M.; Zhuang, K.; Zhao, T.; Chen, X.; Xue, J.; Qiao, Z.; Cui, S.; Gao, Y. Bus Voltage Control of Photovoltaic Grid Connected Inverter Based on Adaptive Linear Active Disturbance Rejection. *Energies* **2022**, *15*, 5556. [[CrossRef](#)]
43. De Nardo, A.; Di Capua, G.; Femia, N. Transformer Design for Isolated Switching Converters Based on Geometric Form Factors of Magnetic Cores. *IEEE Trans. Ind. Electron.* **2012**, *60*, 2158–2166. [[CrossRef](#)]
44. Chen, M.; Loh, P.C. A Dual-Boost H-Bridge Inverter with Common Ground for Photovoltaic Interfacing. *IEEE Trans. Ind. Electron.* **2020**, *68*, 9515–9526. [[CrossRef](#)]

**Disclaimer/Publisher’s Note:** The statements, opinions and data contained in all publications are solely those of the individual author(s) and contributor(s) and not of MDPI and/or the editor(s). MDPI and/or the editor(s) disclaim responsibility for any injury to people or property resulting from any ideas, methods, instructions or products referred to in the content.